Journal of Advanced Ceramics
先进陶瓷
ISSN 2226-4108
CN 10-1154/TQ
清华大学出版社 Tsinghua University Press
SciOpen

J Adv Ceram 2026, **15**: 9221321

https://doi.org/10.26599/JAC.2026.9221321

Research Article

Superior energy storage performance in lead-free $NaNbO_3$-based multilayer ceramic capacitors enabled by relaxor-to-superparaelectric crossover

Zehao Li[1,†], Jianan Zuo[2,†], Xiang Wu[1], Qinkang Jiang[1], Xingan Wang[1], Ao Tian[1], Peiyao Zhao[2], Aiwen Xie[1,*], Xiaohui Wang[2,*]

[1] *Center for Advanced Ceramics, School of Materials Science and Engineering, Anhui Polytechnic University, Wuhu 241000, China*

[2] *State Key Laboratory of New Ceramic Materials, School of Materials Science and Engineering, Tsinghua University, Beijing 100084, China*

† Zehao Li and Jianan Zuo contributed equally to this work.

*Corresponding author.

E-mail: A. Xie, xieaiwen@ahpu.edu.cn;

X. Wang, wxh@mail.tsinghua.edu.cn

Received: February 15, 2026; Revised: April 15, 2026; Accepted: May 13, 2026

Abstract: Dielectric ceramic capacitors are promising for pulsed-power electronics owing to their high-power density and rapid charge/discharge, yet their wider application is limited by a relatively low recoverable energy density (W_{rec}) and the difficulty in simultaneously achieving high W_{rec} and high energy efficiency (η). Herein, a relaxor-to-superparaelectric crossover is engineered in $NaNbO_3$-$(Bi_{0.5}K_{0.5})TiO_3$-$BaZrO_3$ multilayer ceramics, yielding an impressive W_{rec} of ~16.5 J·cm^{-3}, a superior η of ~96.2% and a large W_{rec}/E merit value of 206.3 J·(kV)$^{-1}$·mm^{-2}. Multiscale structural analysis reveals that the introduced $(Bi_{0.5}K_{0.5})TiO_3$ and $BaZrO_3$ stabilize the ferroelectric phase, disrupt long-range polar order, and shift the dielectric permittivity maximum close to room temperature, collectively creating a relaxor-superparaelectric transitional state composed of heterogeneous polar nanoregions (PNRs) with diverse symmetries and sizes. These PNRs exhibit highly dispersive reorientation dynamics under electric fields, and thus enable high maximum polarization and simultaneously minimum hysteresis, accounting for the concurrent enhancement in both W_{rec} and η. Furthermore, the broad thermal stability range of this transitional state leads to excellent temperature-insensitive performance from 25 to 150 ºC (W_{rec} = 8.5 J·cm^{-3}±3.2%, η = 96.1±2.8%). This work demonstrates a viable material strategy of engineering relaxor-superparaelectric crossover to develop high-performance dielectric ceramics for advanced energy storage.

Keywords: lead-free ceramics; $NaNbO_3$-based; relaxor ferroelectric; dielectric energy-storage; heterogeneous nanodomain.

1 Introduction

Dielectric ceramic capacitors are highly promising for pulsed-power systems due to their ultrahigh power density and extremely fast charge-discharge speeds [1−4]. However, their wider application is limited by a relatively low recoverable energy-storage density (W_{rec}). Equally important are high energy-storage efficiency (η) and good temperature stability, which are essential for ensuring

energy-efficient operation, long-term reliability, and device longevity. Therefore, achieving an optimal balance among W_{rec}, η, and thermal stability remains a central challenge in the development of dielectric capacitors [5−8].

Energy-storage performance is commonly evaluated from polarization-electric field (*P*-*E*) hysteresis loops [9−11], according to which materials with high maximum polarization (P_{max}), high breakdown strength (E_B), and low polarization hysteresis generally deliver superior energy-storage properties [12,13]. As a result, ferroelectric (FE) and antiferroelectric (AFE) ceramics have been extensively studied for energy storage owing to their large spontaneous polarizations. A widely adopted strategy to improve their performance involves introducing relaxor characteristics to create nanoscale FE/AFE domains [13−16]. Nevertheless, in relaxor AFEs, the field-induced AFE−FE phase transition is often accompanied by pronounced hysteresis and large switching currents, which degrade η and E_B [17−19]. In contrast, relaxor FEs with highly dynamic polar nanoregions (PNRs) exhibit faster polarization response and consequently lower hysteresis [13,20,21]. As illustrated in the typical dielectric permittivity (ε_r) versus temperature spectrum of relaxor FEs (Fig. 1(a)), they show diffuse temperature-induced phase transition with obvious frequency dispersion. Generally, as temperature increases, the domain size decreases and the dynamics strengthen, leading to reduced polarization hysteresis. Considerable efforts have therefore been directed toward shifting this high-temperature state to room temperature through compositional design, typically by lowering the temperature of the dielectric maximum (T_m) below room temperature to achieve a "superparaelectric state" composed of unit-cell-scale polar clusters. This approach has demonstrated notable performance benefits in both bulk ceramics and thin films. However, the reduction in domain size is often accompanied by a decrease in P_{max}, resulting in a well-known trade-off between η and W_{rec}. Recent multi-strategy designs, such as engineering multiple FE phases, high-entropy design, defect engineering, antiferrodistortion tailoring, and constructing dipole-glass state, have made significant progress in maintaining high P_{max} while suppressing hysteresis [4,7,22−27]. Despite these advances, achieving a comprehensive

performance profile that harmonizes high W_{rec}, high η, and good stability remains a formidable challenge.

To address this challenge, we propose a strategy that designs a relaxor-superparaelectric transition state to achieve an ideal polarization-field response for capacitive energy storage. This state, situated near T_m, combines large-sized, highly polarized PNRs and small-sized, highly dynamic PNRs, thereby facilitating concurrent high P_{max} and low polarization hysteresis. However, the narrow temperature range over which these states typically coexist is detrimental to temperature-stable performance. We therefore further enhance structural fluctuations by introducing local multi-phase coexistence (Fig. 1(b)) [28], which broadens the relaxor-superparaelectric transition and extends the operational temperature window. This design concept has been implemented in this work in lead-free ceramics based on $NaNbO_3$ (NN) by incorporating $Bi_{0.5}K_{0.5}TiO_3$ (BKT) and $BaZrO_3$ (BZ). The selection of NN as the matrix is motivated by its wide band gap (E_g ~3.4 eV) [22,29], which renders it a promising base for constructing dielectric systems with high E_B. However, pure NN ceramic presents a low E_B (~16 $kV \cdot mm^{-1}$) owing to grain coarsening, low density and, especially, easy phase transition between its AFE orthorhombic (O) phase and FE O phase at room temperature because of their similar free energy [22,30]. The introduction of BKT and BZ serves a dual role: thermodynamically, they increase the energy difference between the AFE and FE phases, thereby stabilizing the FE phase (making local ferroelectric distortions more favorable). At the microstructural level, the compositional fluctuations and random fields introduced by BKT and BZ disrupt long-range dipolar ordering, inhibit the formation of macroscopic domains, and instead stabilize a nanoscale heterogeneous polar state consisting of PNRs with diverse symmetries and sizes. Specifically, BKT inherently possesses a tetragonal (T) FE structure with space group *P*4*mm* at room temperature [31], while BZ has been reported to induce a rhombohedral (R) phase (*R*3*c*) in NN-based solid solutions [32], thereby promoting the desired polymorphic nanodomain structure [32−34]. As a result, the NN-BKT-BZ bulk ceramics exhibit significantly enhanced energy-storage performance, with $W_{rec} \approx 9.4$ $J \cdot cm^{-3}$ and $\eta \approx$

88.8% (Fig. 1(c)). More importantly, the corresponding multilayer ceramic capacitors (MLCCs) achieve an outstanding $W_{rec} \approx 16.5$ J·cm^{-3} along with a remarkably high $\eta \approx 96.2\%$, demonstrating pronounced advantages for practical dielectric energy-storage applications.

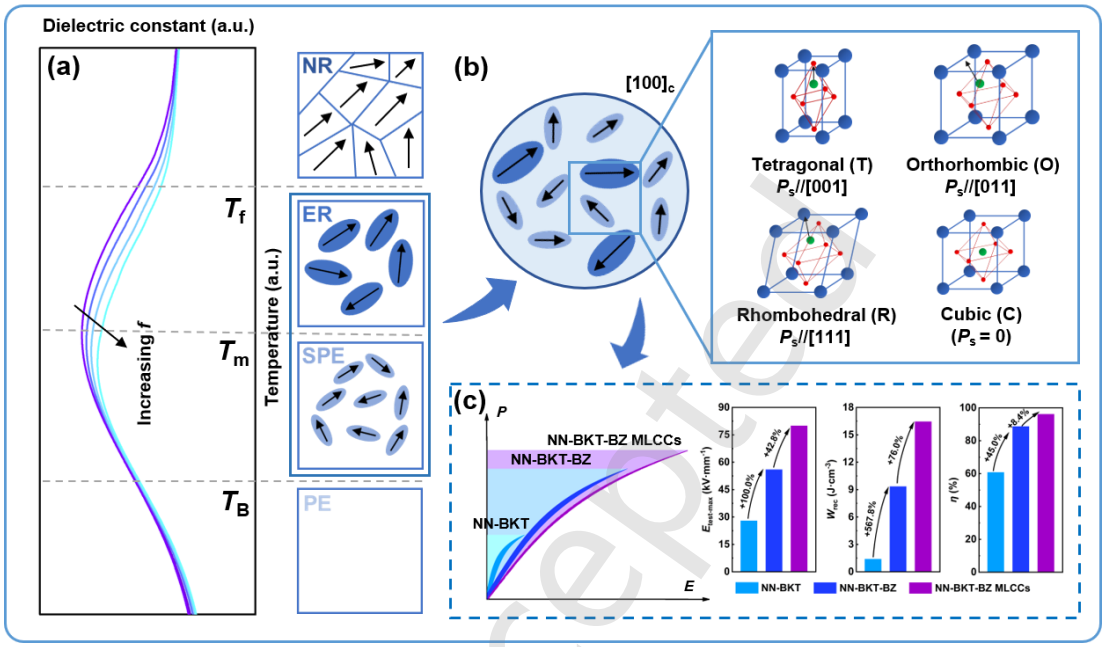

Fig. 1 Schematic of the design strategy for high-performance NN-BKT-BZ ceramic capacitors. (a) The sketch of the temperature-dependent dielectric response for typical relaxor Fes (NR: nonergodic relaxor, ER: ergodic relaxor, SPE: superparaelectric, PE: paraelectric; T_f: freezing temperature, T_B: Burn temperature). (b) Schematic of synergistic coexistence of polymorphic (T/O/R/C) domain structures. (c) Energy storage performance comparison of NN-BKT, NN-BKT-BZ bulk ceramics and NN-BKT-BZ MLCCs.

2 Experiment and characterizations

(0.8-x)NN-0.2BKT-xBZ (x = 0−0.12) ceramics were prepared by a conventional solid phase reaction method using high-purity (> 99%) Na_2CO_3, Nb_2O_5, Bi_2O_3, K_2CO_3, TiO_2, $BaCO_3$, ZrO_2. The mixtures of the weighed raw powders were ball milled in ethanol with zirconia balls for 6 hours. The dried powders were calcined at 850 ºC for 5 hours in a covered alumina crucible and then ball milled

again for 8 hours with 0.4 wt% MnO_2 (> 99%) as sintering aids to improve the sintering behavior [35,36]. After that, the obtained powders were pressed into pellets with diameter ~10 mm and sintered in sealed crucibles at 1210−1230 ºC for 2 hours. The ceramic samples were polished to obtain parallel surfaces and coated with silver paste and then fired at 600 ºC for 20 minutes. For dielectric and impedance measurements, the bulk ceramic samples feature a thickness of ~0.7 mm and an electrode area of ~60.8 mm^2, while bulk samples for *P-E* loops, pulse charge-discharge, leakage current and E_B measurements possess an electrode area of ~1.2 mm^2 with a uniform thickness of ~0.1 mm. To fabricate the MLCCs, 100 g of the calcined powder with the $x = 0.06$ composition was dispersed in a dispersant solution (ethyl acetate: 45 g, ethanol: 35 g, dispersant: 2 g) and ball-milled for 12 hours. A binder solution (ethyl acetate: 25 g, ethanol: 10 g, binder: 15 g) and 6 g of plasticizers were subsequently added prior to a further 12 hours milling step. The obtained slurry was first filtered through a 200-mesh filter to remove large agglomerates and impurities, then degassed in a vacuum degasser at 1800 r/min under a vacuum pressure of 13 kPa for 30 minutes to eliminate air bubbles. The degassed slurry was processed via tape-casting using a doctor blade with a gap of 15 μm, at a casting speed of 50 cm/min, to form green sheets. After cutting the green sheets into appropriate sizes, 70Ag/30Pd electrode paste was screen-printed onto these sheets. The printed green sheets were then stacked in a predetermined order according to the MLCC design, followed by lamination in a hot press at 50 ºC and 5 MPa for 5 minutes. To further enhance the green density and eliminate interlayer gaps, the stacked laminates were subjected to warm isostatic pressing at 55 ºC and 50 MPa for 10 minutes. After cutting the green laminate into pieces of 4.2 × 3.8 mm, thermal debinding was performed at 600 °C for 2 h with a heating rate of 0.5 °C/min to remove the organic binders. Finally, the MLCCs were sintered at 1210 ºC for 2 hours. The MLCC samples in this work contain 5 dielectric layers, with a thickness of ~12 μm per layer and a total electrode area of ~8 mm^2.

Detailed procedures for structural characterizations and electrical performance tests can be found in our previous work [7].

3 Results and discussion

Fig 2(a) shows the X-ray diffraction (XRD) patterns of (0.8-*x*)NN-0.2BKT-*x*BZ ceramics. All compositions crystallize in a pure perovskite structure without detectable secondary phases, confirming successful single-phase synthesis. The incorporation of BZ, where larger Zr^{4+} ions (R_{Zr} = 0.72 Å, CN = 6) substitute for Nb^{5+} (R_{Nb} = 0.64 Å) [37], induces a lattice expansion, as evidenced by the gradual shift of the (200) diffraction peak toward lower angles with increasing *x*. Rietveld refinements of the XRD patterns for the (0.8-*x*)NN-0.2BKT-*x*BZ compositions are shown in Figs. 2(b)-(c) and Fig. S1 in the Electronic Supplementary Material (ESM). The single characteristic diffraction peaks in the XRD patterns indicate that the average structure of all compositions remains pseudo-cubic. Conventional XRD is inherently limited in resolving the local symmetry of PNRs in relaxor FEs. Therefore, we refined the XRD data for all compositions using the cubic $Pm\bar{3}m$ space group [38]. The goodness-of-fit factors (R_{wp}, R_p, and χ^2) obtained from the refinements confirm good reliability of the structural models. Detailed refined crystallographic parameters are shown in Table S1 and S2 (ESM). The local structural influence of BZ doping was further probed by Raman spectroscopy (Fig. 2(d)). The intensities of the v_5 (B-O stretching) and v_1 (BO_6 octahedral) modes progressively decrease and broaden with higher BZ content [22,24,39], suggesting enhanced structural disorder and reduced lattice polarity. This evolution toward a more disordered state is consistent with the dielectric behavior. As shown in Fig. 2(e) and Fig. S2 in the ESM, increasing the BZ content leads to more pronounced frequency dispersion and a broadening of the dielectric permittivity peak. This indicates strengthened relaxor characteristics, stemming from disrupted long-range polar order and enhanced local compositional heterogeneity [40]. The trend is quantified by an increase in both the diffuseness exponent (γ), derived from a modified Curie-Weiss law (Fig. 2(f)), and the relaxation factor ΔT_{relax} (the difference between T_m at 1 MHz and 1 kHz, Fig. 2(g)). These parameters confirm a more diffuse temperature-induced relaxor-to-superparaelectric transition. Concurrently, the T_m shifts downward as

long-range ferroelectric order is disrupted [15,20]. For the x = 0.06 composition, room temperature lies between its T_m measured at 1 kHz and 1 MHz (Fig. 2(h)), confirming the stabilization of a relaxor-superparaelectric crossover state under ambient conditions.

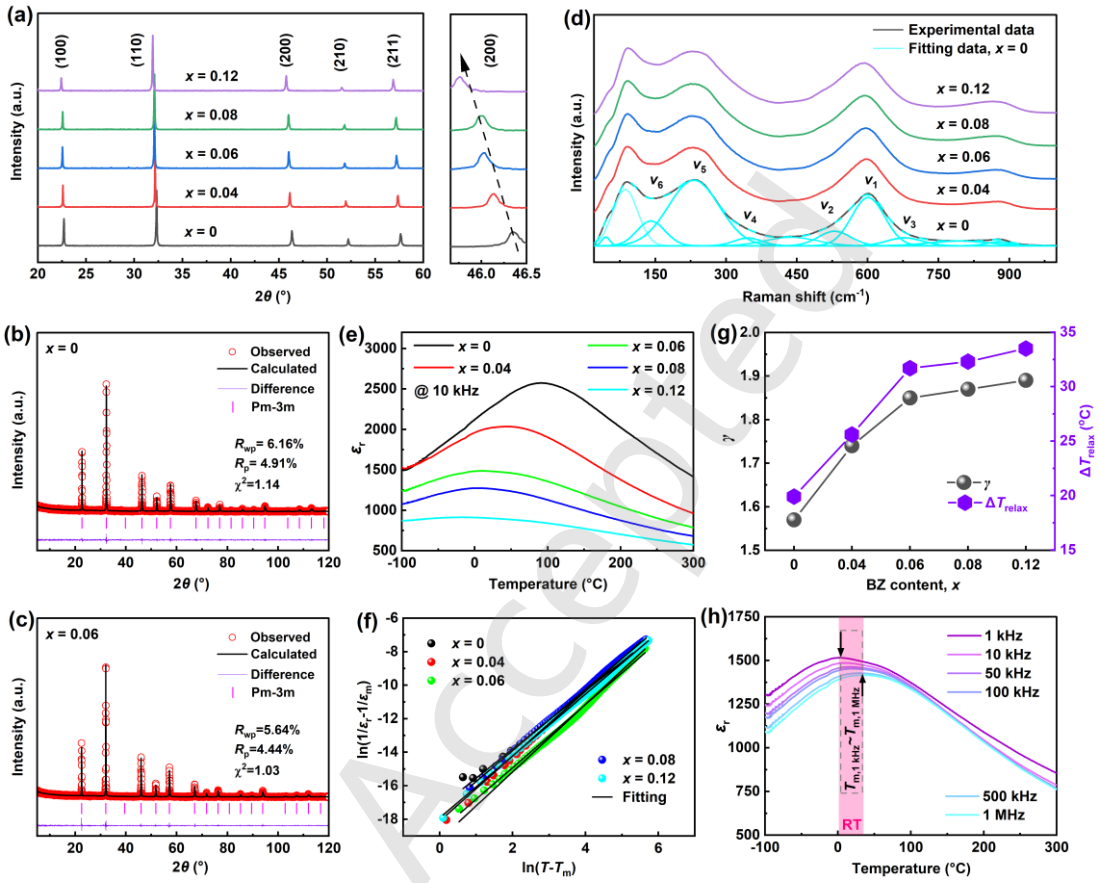

Fig. 2 (a) XRD patterns with enlarged (200) peaks of the (0.8-x)NN-0.2BKT-xBZ ceramics and Rietveld refinement results for (b) x = 0 and (c) x = 0.06 ceramics. (d) Raman spectra of the (0.8-x)NN-0.2BKT-xBZ ceramics. (e) Temperature-dependent ε_r of the (0.8-x)NN-0.2BKT-xBZ ceramics under 10 kHz measured on heating. (f) Correlation between $\ln(1/\varepsilon_r-1/\varepsilon_m)$ and $\ln(T-T_m)$. (g) γ and ΔT_{relax} values as a function of x. (h) Temperature and frequency dependence of ε_r for the x = 0.06 ceramics.

The evolution of domain morphology was investigated via piezoresponse force microscopy (PFM). While the x = 0 ceramic exhibits distinct regions with strong piezoelectric contrast indicative of well-defined ferroelectric domains, the x = 0.06 and x = 0.12 compositions show featureless patterns with inconspicuous domain contrast (Figs. 3(a)−3(c)). This signifies a significant reduction in domain

size and the formation of PNRs [7]. The progressive decrease in piezoresponse amplitude with increasing BZ content is attributed to enhanced interactions with local random fields. These microstructural changes profoundly affect the macroscopic polarization response. Under a fixed electric field of 15 kV·mm^{-1}, the *P*-*E* loops become progressively slimmer with higher BZ content, reflecting the enhanced dynamics of the smaller polar domains (Fig. 3(d)). Both the P_{max} and remnant polarization (P_r) decrease. For compositions with $x \geq 0.06$, ΔP (P_{max}-P_r) nearly equals P_{max}, indicating minimal hysteresis (Fig. 3(e)). Consequently, the η rises from 67% ($x = 0$) to 95% ($x = 0.12$), while the W_{rec} first increases and then decreases (Fig. 3(f)). An optimal balance is achieved at $x = 0.06$, with W_{rec} ≈ 1.0 J·cm^{-3} and $\eta \approx 93.0\%$.

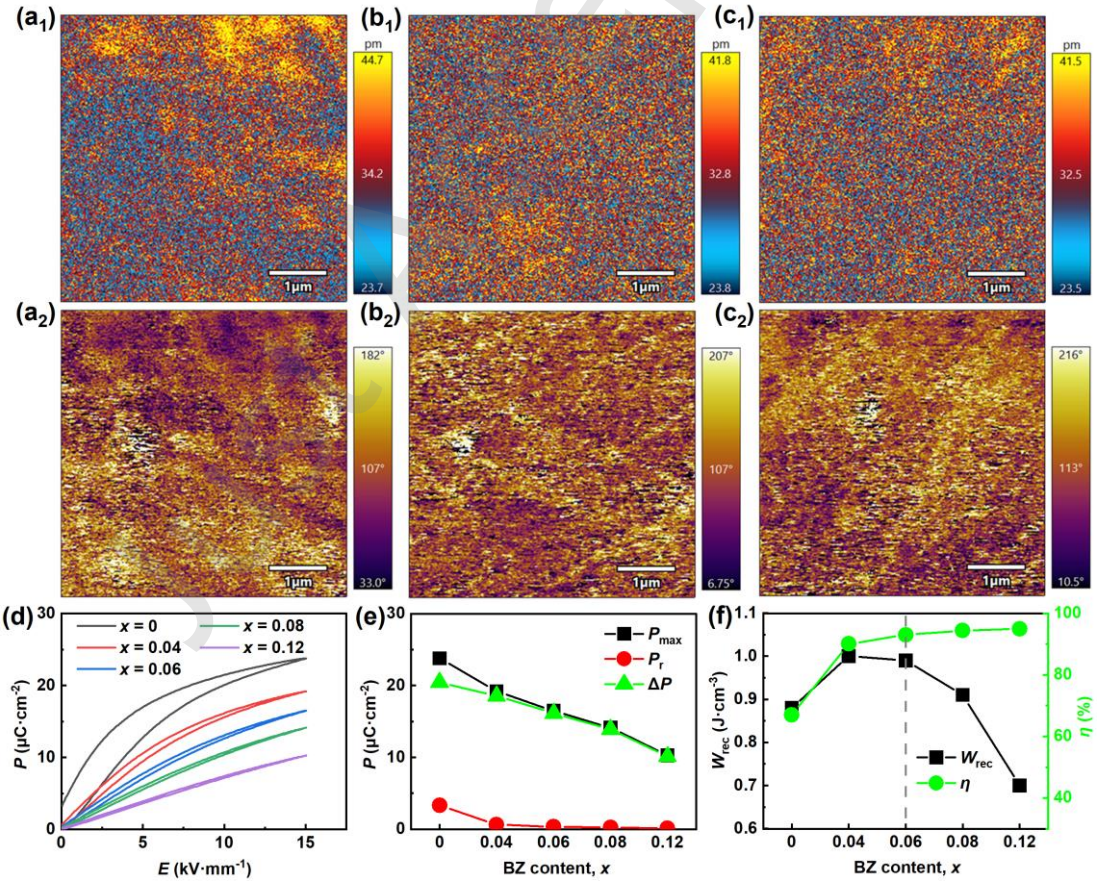

Fig. 3 Out-of-plane PFM amplitude (subscript 1) and phase (subscript 2) images for the (0.8-*x*)NN-0.2BKT-*x*BZ ceramics measured under 10 V: (a_1, a_2) $x = 0$, (b_1, b_2) $x = 0.06$ and (c_1, c_2) $x = 0.12$. (d)

P-E loops under 15 kV·mm^{-1} and 10 Hz, (e) P_{max}, P_r and ΔP values and (f) the obtained W_{rec}, η values of the (0.8-*x*)NN-0.2BKT-*x*BZ ceramics.

Transmission Electron Microscopy (TEM) was conducted on the x = 0.06 ceramic to gain an atomic-scale insight into the polar structure underpinning the relaxor-superparaelectric crossover. Bright-field TEM images show no discernible contrast for long-range FE domains across diverse grains, suggesting the predominance of PNRs (Figs. 4(a) and 4(b)). Selected area electron diffraction (SAED) patterns along the $[100]_c$ and $[110]_c$ zones (Figs. 4(c) and 4(d)) show sharp diffraction spots, confirming excellent crystallinity. In NN system, 1/4- and 1/6-type superlattice spots are characteristic signatures of the two AFE O phases, which possess four and six basic perovskite cubic cells, respectively [41,42], while 1/2-type superlattice spots correspond to the FE phases [43]. The exclusive presence of 1/2-type superlattice spots and the absence of 1/4- and 1/6-type reflections thus confirm the FE symmetry and rule out any AFE phase. Specifically, the observed 1/2(100) and 1/2(110) superlattice reflections originate from the O phase in the $NaNbO_3$ system, which features a doubled supercell induced by characteristic oxygen octahedral tilting and lattice modulation [42]. This SAED analysis therefore provides rigorous crystallographic evidence that the FE phase is stabilized, without long-range AFE order. Atomic-resolution high-angle annular dark-field scanning TEM (HAADF-STEM) image along $[100]_c$ reveals the polarization vectors (Fig. 4(e)). Regions with polarization aligned along <001> and <110> correspond to T and O/R phases, respectively [7,44], while areas with ultra-weak polarization are identified as cubic (C) phases. This coexistence of multiple local symmetries, together with the island-like clusters of varied sizes visible in the polarization-magnitude and polarization-angle mappings (Figs. 4(f) and 4(g)), confirms a nanoscale heterogeneous architecture. Critically, the embedding of T and O/R phases within a weakly polar matrix gives rise to a bimodal distribution of PNRs: larger PNRs (~4 nm) that provide substantial polarization and smaller, highly dynamic PNRs (~1 nm) that facilitate rapid reorientation. This multiscale PNR ensemble is a hallmark of the relaxor-superparaelectric transitional state, which enables diffuse domain switching under an

electric field, thereby minimizing polarization hysteresis while retaining a high P_{max}. In-situ PFM observations under varying driving voltages further elucidate the dynamic behavior (Fig. 4(h)). With increasing voltage, the piezoresponse amplitude rises, indicating progressive alignment of PNRs along the field direction. At low fields (10−30 V), fine, irregular dot-like domains are observed, consistent with the response of isolated PNRs. At 40 V, some regions develop distinct stripe-like domains, suggesting slight field-induced coalescence or growth of PNRs [15]. Notably, different areas exhibit distinct domain-evolution pathways, underscoring the spatial heterogeneity of the nanodomain configuration [14,45]. Most importantly, upon removal of the electric field, the domain pattern rapidly reverts to its initial dot-like morphology (Fig. S3 in the ESM), demonstrating fast and fully reversible switching.

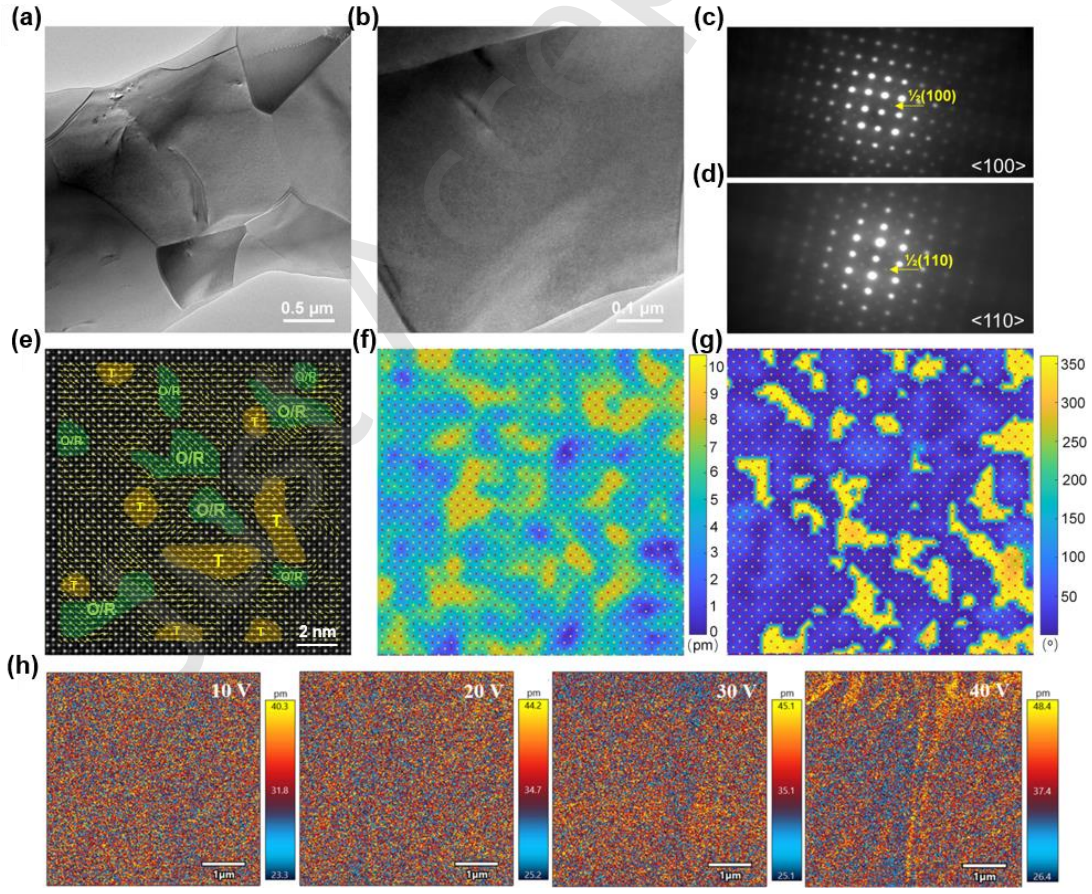

Fig. 4 (a, b) Bright-field TEM image and corresponding (c, d) SAED patterns in diverse regions, (e) Atomic-resolution HAADF-STEM polarization vector images as well as (f) the polarization magnitude

and (g) polarization angle mappings, (h) Out-of-plane PFM amplitude images measured under 10 V−40 V voltages of the $x = 0.06$ ceramics.

E_B is also a critical factor governing energy-storage performance. Impedance spectroscopy was employed to understand electrical conduction and relaxation. The Nyquist plots (Z' vs. Z'') measured at 500 °C (Fig. 5(a)) show near-single semicircular arcs for all compositions. These plots were well-fitted using an equivalent circuit composed of two series-connected resistor-constant phase elements (R-CPE), representing contributions from the grain and grain boundary, respectively. The observed single semicircle arises from the overlap of the two electrical processes within the measured frequency range. The fitted total resistivity (ρ_{total}) increases markedly with BZ content (Fig. 5(b)), primarily due to an increased proportion of high-resistivity grain boundaries resulting from grain refinement (Figs. S4(a)−S4(f) in the ESM) [39,46]. Importantly, the ceramic samples achieve high densification with negligible porosity (relative density > 96%) and uniform distribution of elements (Fig. S4(g) in the ESM), ensuring reliable microstructure and electrical property analysis. To further clarify the electrical conduction mechanism, impedance spectra of all compositions were measured and analyzed, and the corresponding activation energy (E_a) was calculated based on the Arrhenius relation [47] (Fig. S5 in the ESM). It was observed that E_a increases with rising BZ content, indicating an elevated energy barrier for charge carrier migration. This trend contributes to the suppression of leakage current density and facilitates the achievement of a higher E_B. The normalized imaginary impedance (Z''/Z''_{max}) versus frequency for the $x = 0.06$ ceramic shows a single relaxation peak that shifts to higher frequencies with increasing temperature (400−550 °C, Fig. 5(c)), indicating defect- and vacancy-related mechanisms dominate the temperature-dependent dielectric relaxation [48]. Additionally, the optical E_g, a key intrinsic parameter related to E_B, was evaluated from UV-Vis spectra using the Tauc relation [49]. E_g increases from 3.07 eV ($x = 0$) to 3.15 eV ($x = 0.06$), and reaches a maximum of 3.20 eV ($x = 0.12$) (Fig. 5(d)), suggesting enhanced intrinsic E_B. The concurrent rise in resistivity and E_g effectively suppresses leakage current density (Fig. 5(e)), thereby promoting a higher E_B. The characteristic E_B

was statistically determined via Weibull distribution analysis (Fig. 5(f)) [50]. Linear fits yield shape parameters (m) > 10, confirming high data reliability. As summarized, E_B increases substantially from 28.6 kV·mm^{-1} (x = 0) to 57.3 kV·mm^{-1} (x = 0.06), and the upward trend gradually moderates at x > 0.06, finally reaching a maximum of 62.5 kV·mm^{-1} (x = 0.12).

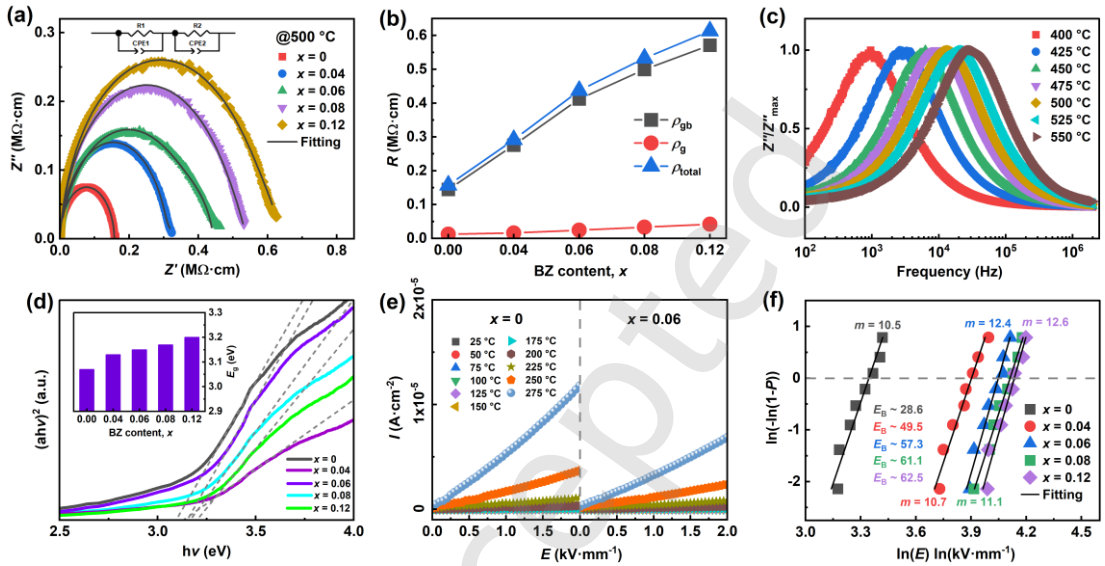

Fig. 5 (a) Complex AC impedance tested at 500 °C, and the corresponding fitting data were analyzed using an equivalent fitting circuit composed of two series-connected R-CPE units, representing the contributions from grain and grain boundary, respectively. (b) ρ_{gb}, ρ_g and ρ_{total} values from the fitting results of the (0.8-x)NN-0.2BKT-xBZ ceramics and (c) frequency-dependent Z''/Z''_{max} in the temperature range of 400−550 °C of the x = 0.06 ceramics. (d) Energy dependence of $(\alpha h\nu)^2$ and the corresponding E_g for the (0.8-x)NN-0.2BKT-xBZ ceramics, (e) temperature-dependent leakage current of x = 0 and x = 0.06 ceramics and (f) the Weibull distribution and corresponding E_B (kV·mm^{-1}) for the (0.8-x)NN-0.2BKT-xBZ ceramics.

The energy-storage performance of the optimized x = 0.06 ceramic under varying electric fields is shown in Fig. 6. With increasing field, P_{max} rises from 13.6 to 52.7 μC·cm^{-2}, while P_r remains low (< 3 μC·cm^{-2}) across 10−56 kV·mm^{-1} (Fig. 6(a)). The corresponding current density-electric field (J-E) curves exhibit a smooth plateau (Fig. 6(b)), indicative of a diffuse domain-switching process arising from the heterogeneous PNR structure with varied symmetries and sizes. Consequently, W_{rec} increases

nearly linearly with the field, reaching an optimum of ≈ 9.4 J·cm^{-3} with $\eta \approx 88.8\%$ at 56 kV·mm^{-1} (Fig. 6(c)). Fig. 6(d) compares the W_{rec} versus electric field of the $x = 0.06$ ceramic with other lead-free bulk ceramics [6,51−55], highlighting its superior performance at comparable fields. Furthermore, the ceramic exhibits excellent pulse charge-discharge characteristics (Figs. 6(e) and 6(f)). Under 40 kV·mm^{-1}, it delivers a discharge energy density (W_D) of 5.7 J·cm^{-3}, a power density (P_D) of 252.1 MW·cm^{-3}, and an ultrafast discharge time ($t_{0.9}$) below 35 ns. This exceptional charge-discharge performance stems from the synergistic regulation of the heterogeneous PNRs architecture and refined microstructure. Larger PNRs with high polarization magnitude furnish the sufficient polarization required to secure a high W_D, while smaller PNRs with ultrahigh dynamic responsiveness enable rapid and reversible polarization switching, thus realizing an ultrafast $t_{0.9}$ and high P_D. In addition, the improved microstructure effectively reduces leakage current and improves resistance, further optimizing the charge-discharge efficiency of the ceramic.

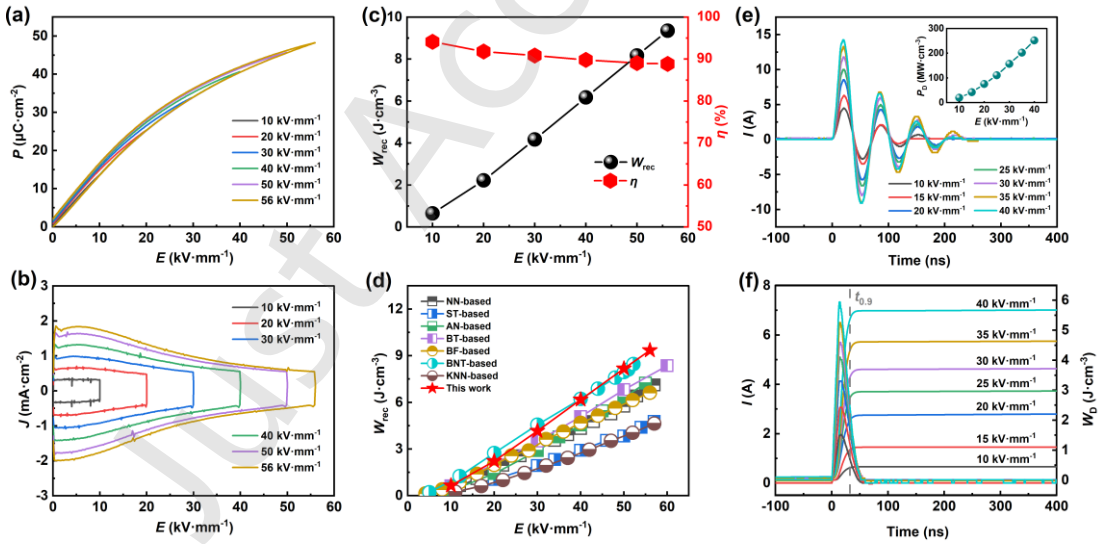

Fig. 6 (a) *P-E* loops, corresponding (b) *J-E* curves, and (c) W_{rec}, η values measured under different electric fields and 10 Hz of the $x = 0.06$ ceramics. (d) Comparison of energy storage properties between the $x = 0.06$ ceramics and other lead-free energy storage ceramics [6,51−55]. Room-temperature (e) underdamped *I-t* curves with corresponding P_D values, (f) overdamped *I-t* curves with corresponding W_D values of $x = 0.06$ ceramics at different electric fields.

Owing to the superior comprehensive energy-storage performances, an MLCC device was fabricated using the x = 0.06 composition to exploit its full potential. A cross-sectional SEM image (Fig. 7(a)) reveals five dense dielectric layers (~12 μm each) alternating with well-defined electrode layers (~2 μm). The five-layer structure was chosen considering both the feasibility of experimental fabrication and the purpose of demonstrating application potential. As an academic study conducted with laboratory-scale equipment, fabricating MLCCs with more than ten layers would introduce a high risk of structural defects, delamination, or short circuits during co-firing, which would severely degrade the E_B and energy-storage performance. On the other hand, using too few layers (e.g., single- or double-layer) cannot fully reflect the structural advantages of MLCCs and would limit the effective discharge energy output. Therefore, five layers were selected as a reasonable and representative compromise that balances processability, structural stability, and energy-storage performance. The average grain size in the MLCC is notably smaller than in the bulk ceramic (Fig. S4 in the ESM), attributable to differences in the sintering process. However, the temperature-dependent dielectric property of the MLCC sample (Fig. S6(a)) demonstrates the construction of a relaxor-superparaelectric transition state at room temperature, which is consistent with the results of bulk ceramics. As a result, the MLCC exhibits excellent energy-storage properties. Its *P*-*E* loops show extremely low hysteresis, while a high P_{max} of ~55.2 μC·cm^{-2} is achieved at 80 kV·mm^{-1} (Figs. 7(b) and 7(c)). This results in remarkable parameters of W_{rec} = 16.5 J·cm^{-3} and η = 96.2% at this field (Fig. 7(d)). The higher η compared to the bulk counterpart is likely associated with grain refinement and improved electrode-dielectric interfaces in the multilayer configuration [2,56]. A performance comparison with recently reported MLCCs [2,7,54,55,57−64] shows that the present MLCC holds a distinct advantage in simultaneously achieving high W_{rec} and high η (Figs. 7(e) and 7(f)). Its merit index, W_{rec}/E, reaches ~206.3 J·(kV)$^{-1}$·mm^{-2}, surpassing most counterparts. We note that the testing conditions and structural parameters of the referenced MLCCs are not identical (e.g., dielectric layer thickness varies across different studies). To ensure a transparent and fair comparison, we have listed the key parameters—

including the number of layers, single-layer thickness, and reported energy-storage performance—for all compared MLCCs in Table S3. Also, to provide a broader perspective on testing configurations, we have also summarized the electrode areas and sample thicknesses of selected single-layer bulk ceramics alongside the parameters of our MLCC in Table S4. Furthermore, the MLCC exhibits excellent discharge performance, with a peak P_D of ~273.4 MW·cm^{-3}, a maximum W_D of ~8.4 J·cm^{-3}, and an ultrafast $t_{0.9}$ of ~0.67 μs at 50 kV·mm^{-1} (Figs. 7(g)−7(i)), demonstrating its great potential for practical high-power energy storage applications.

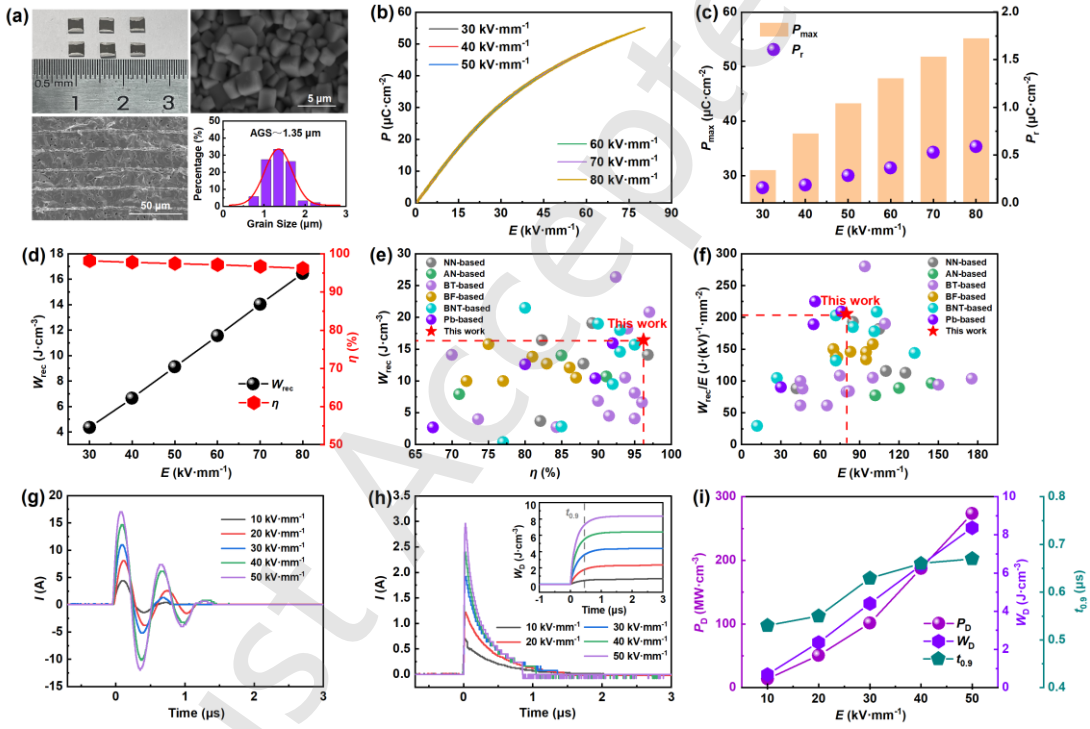

Fig. 7 (a) Optical photograph, cross-sectional SEM image and surface SEM image with the corresponding grain size distribution of the x = 0.06 MLCCs. (b) *P*-*E* loops with (c) corresponding P_{max}, P_r values, and (d) W_{rec}, η values measured under different electric fields and 10 Hz of the x = 0.06 MLCCs. (e) A comparison of W_{rec} and η values between the x = 0.06 MLCCs and other recently-reported MLCCs [2,7,54,55,57−64]. (f) A comparison of W_{rec}/E values between the x = 0.06 MLCCs and other recently-reported MLCCs [2,7,54,55,57−64]. (g) Underdamped *I*-*t* curves, (h) overdamped *I*-*t* curves with corresponding W_D *vs.* time curves, (i) P_D, W_D, and $t_{0.9}$ as a function of electric field for x = 0.06 MLCCs.

The stability of the energy-storage performance is equally critical. *P-E* loops measured from 25 to 125 °C retain low hysteresis with only minor variation in P_{max} (Fig. 8(a)), yielding temperature-insensitive performance: $W_{rec} \approx 8.5\pm3.2\%$ J·cm^{-3} and $\eta \approx 96.1\pm2.8\%$ at 50 kV·mm^{-1} (Fig. 8(b)). This excellent thermal stability originates from the broad relaxor-to-superparaelectric crossover regime where polymorphic PNRs persist, as supported by temperature-invariant Raman spectra (Fig. S7 in the ESM) and outstanding temperature stability of dielectric property (Fig. S6(b) in the ESM). The capacitance variation requirements of the X8R specification further confirm the reliability of the material for high-temperature MLCC applications. Moreover, the MLCC exhibits frequency-stable *P-E* loops from 1 to 100 Hz (Fig. 8(c)), attributable to the highly dynamic PNRs enabling rapid polarization response. Consequently, consistent performance is maintained over this frequency range: $W_{rec} \approx 8.5\pm1.8\%$ J·cm^{-3} and $\eta \approx 96.4\pm1.6\%$ (Fig. 8(d)). Notably, the MLCC also demonstrates exceptional cycling stability, with well-preserved *P-E* loops and highly stable energy storage performance even after 10^4 charge-discharge cycles (Fig. 8(e)). The W_{rec} and η remain nearly constant at ~8.4±3.7% J·cm^{-3} and ~96.3±2.2%, respectively, throughout the cycling process (Fig. 8(f)), verifying its long-term operational reliability for practical energy storage applications. This excellent cycling stability is attributed to the highly dynamic nature of nanodomains, which enable fully reversible polarization switching without fatigue-induced structural degradation.

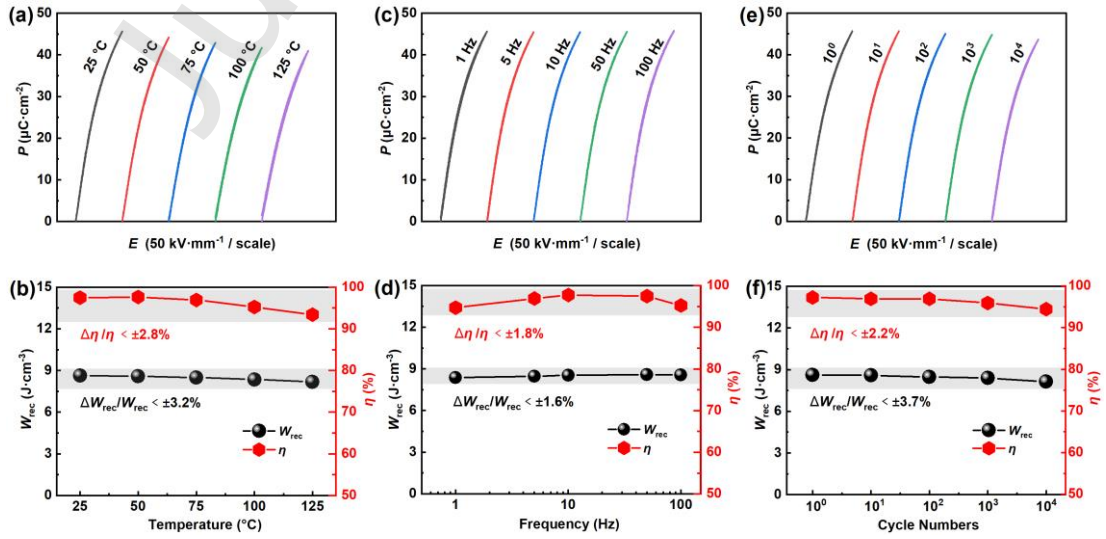

Fig. 8 (a) Temperature-dependent *P-E* loops and (b) corresponding W_{rec}, η values measured at 50 kV·mm^{-1} and 10 Hz, (c) frequency-dependent *P-E* loops and (d) corresponding W_{rec}, η values measured at 50 kV·mm^{-1} and room temperature, (e) cycling-dependent *P-E* loops and (f) corresponding W_{rec}, η values measured at 50 kV·mm^{-1}, room temperature, and 10 Hz of x = 0.06 MLCCs.

4 Conclusions

In summary, by engineering a relaxor-to-superparaelectric crossover, we have developed a lead-free $NaNbO_3$-based ceramic system that achieves superior overall energy-storage performance. Multiscale structural characterizations, including XRD, Raman spectroscopy, PFM, and HAADF-STEM, verify that the incorporation of BKT and BZ disrupts long-range FE order and promotes a heterogeneous domain architecture consisting of both large, highly polarized PNRs and small, highly dynamic PNRs with diverse local symmetries. This distinctive configuration supplies multiple polarization pathways, which effectively suppresses hysteresis while retaining a high P_{max}. The optimized polarization response is directly reflected in outstanding macroscopic properties: the fabricated MLCCs with x = 0.06 exhibit a remarkable W_{rec} of ~16.5 J·cm^{-3} and a near-ideal η of ~96.2% at 80 kV·mm^{-1}, corresponding to an impressive W_{rec}/E merit value of ~206.3 J·(kV)$^{-1}$·mm^{-2}. Moreover, the broad stability range of the designed transitional state ensures excellent temperature resilience between 25 and 125 ºC, with W_{rec} maintained at 8.5±3.2% J·cm^{-3} and η at 96.1±2.8%. These findings establish a viable and generalizable material-design principle for developing high-performance dielectrics for next-generation pulsed-power electronics.

Availability of data and materials

The data that support the findings of this study are available from the corresponding author upon reasonable request.

Competing interests

The authors have no competing interests to declare that are relevant to the content of this article.

Funding

Financial support from the National Natural Science Foundation of China (52302131, 54272130), and the Key Research and Development Program of Anhui Province (202304a05020044, 202423i08050005). The funding bodies played essential roles in the design of the study, collection of experimental data, analysis and interpretation of structural/performance data (including XRD, TEM, and energy storage performance characterization), and writing/revising of the manuscript. All authors confirm that the funding bodies did not impose any restrictions on the design of the study, data analysis, interpretation of results, or the submission of the manuscript for publication.

Author contributions

Conceptualization and supervision (Aiwen Xie and Xiaohui Wang), writing-original draft (Zehao Li, Jianan Zuo, and Aiwen Xie), methodology (Zehao Li, Xiang Wu, Qinkang Jiang, Ao Tian, Peiyao Zhao), investigation (Zehao Li, Jianan Zuo, Aiwen Xie, Xiang Wu and Xingan Wang), supervision (Aiwen Xie, Ao Tian), data curation (Zehao Li, Jianan Zuo and Qinkang Jiang), resources (Aiwen Xie and Xiaohui Wang), writing-review & editing (Aiwen Xie and Xiaohui Wang).

Acknowledgements

Financial support from the National Natural Science Foundation of China (52302131, 52472130), and the Key Research and Development Program of Anhui Province (202304a05020044, 202423i08050005) is gratefully acknowledged.

Electronic Supplementary Material (ESM)

Supplementary material (Fig. S1: Rietveld XRD refinement results, Fig. S2: Temperature-dependent ε_r and tanδ at different frequencies for bulk ceramics, Fig. S3: PFM amplitude image, Fig. S4: SEM micrographs, grain size distributions and elemental mappings, Fig. S5: Complex AC impedance spectra and corresponding E_a, Fig. S6: Temperature and frequency dependence of ε_r and capacitance variation for MLCCs, Fig. S7: Temperature-dependent Raman spectroscopy, Table S1, S2: Structural parameters, atomic positions, and Table S3, S4: key parameters and performance comparisons) is available in the online version of this article.

References

[1] Liu YJ, Zhang Y, Wang J, *et al*. Ultrahigh capacitive energy storage through dendritic nanopolar design. *Science* 2025, **388**: 211–216.

[2] Zhang M, Lan S, Yang BB, *et al*. Ultrahigh energy storage in high-entropy ceramic capacitors with polymorphic relaxor phase. *Science* 2024, **384**: 185–189.

[3] Yang MZ, Guo MF, Xu EX, *et al*. Polymer nanocomposite dielectrics for capacitive energy storage. *Nat Nanotechnol* 2024, **19**: 588–603.

[4] Fu J, Xie AW, Zuo RZ, *et al*. A highly polarizable concentrated dipole glass for ultrahigh energy storage. *Nat Commun* 2024, **15**: 7338.

[5] Shu L, Shi XM, Zhang X, *et al*. Partitioning polar-slush strategy in relaxors leads to large energy-storage capability. *Science* 2024, **385**: 204–209.

[6] Yan F, Qian J, Wang SM, *et al*. Progress and outlook on lead-free ceramics for energy storage applications. *Nano Energy* 2024, **123**: 109394.

[7] Xie AW, Li ZH, Wu X, *et al*. Superior capacitive energy storage of $NaNbO_3$-based MLCCs enabled by heterogeneous short-range ferroic orders. *Adv Funct Mater* 2026, **36**: e16297.

[8] Veerapandiyan V, Benes F, Gindel T, *et al*. Strategies to improve the energy storage properties of perovskite lead-free relaxor ferroelectrics: a review. *Materials* 2020, **13**: 5742.

[9] Park S, Kim S, Lee C, *et al*. A-/B-site engineering of $AgNbO_3$-based ceramics for high-efficiency relaxor antiferroelectric energy storage. *J Adv Ceram* 2025, **14**: 9221174.

[10] Yang LT, Kong X, Li F, *et al*. Perovskite lead-free dielectrics for energy storage applications. *Prog Mater Sci* 2019, **102**: 72–108.

[11] Yang KH, Luo GG, Ma L, *et al*. Excellent energy storage performance in $Bi_{0.5}Na_{0.5}TiO_3$-based lead-free high-entropy relaxor ferroelectrics via B-site modification. *J Adv Ceram* 2024, **13**: 345–353.

[12] Yang ZT, Du HL, Jin L, *et al*. High-performance lead-free bulk ceramics for electrical energy storage applications: design strategies and challenges. *J Mater Chem A* 2021, **9**: 18026–18085.

[13] Cao WJ, Lin RJ, Hou X, *et al*. Interfacial polarization restriction for ultrahigh energy-storage density in lead-free ceramics. *Adv Funct Mater* 2023, **33**: 2301027.

[14] Xie AW, Zuo RZ, Qiao ZL, *et al*. $NaNbO_3$-$(Bi_{0.5}Li_{0.5})TiO_3$ lead-free relaxor ferroelectric capacitors with superior energy-storage performances via multiple synergistic design. *Adv Energy Mater* 2021, **11**: 2101378.

[15] Zhou SY, Zhou YC, Li LH, *et al*. Ultrawide-temperature-stable high-entropy relaxor ferroelectrics for energy-efficient capacitors. *Nat Commun* 2025, **16**: 8456.

[16] Ma JJ, Zhang DH, Ying F, *et al*. Ultrahigh energy storage density and high efficiency in lead-free $(Bi_{0.9}Na_{0.1})(Fe_{0.8}Ti_{0.2})O_3$-modified $NaNbO_3$ ceramics via stabilizing the antiferroelectric phase and enhancing relaxor behavior. *ACS Appl Mater Interfaces* 2022, **14**: 19704–19713.

[17] Mandal A, Yadav KK. Significant advancements in energy density of NN-based anti-ferroelectric material: A breakthrough in low electric field region design strategies. *Chem Eng J* 2025, **504**: 158942.

[18] Li JL, Li F, Xu Z, *et al*. Multilayer lead-free ceramic capacitors with ultrahigh energy density and efficiency. *Adv Mater* 2018, **30**: 1802155.

[19] Dou ZM, Wang W, Zhang YY, *et al*. Improving energy density and efficiency in antiferroelectric-based multilayer ceramic capacitors via composition design engineering. *Ceram Int* 2025, **51**: 8454–8464.

[20] Li D, Zhou D, Wang D, *et al*. Improved energy storage properties achieved in $(K,Na)NbO_3$-based relaxor ferroelectric ceramics via a combinatorial optimization strategy. *Adv Funct Mater* 2022, **32**: 2111776.

[21] Sun ZX, Wang Z, Tian Y, *et al*. Progress, outlook, and challenges in lead-free energy-storage ferroelectrics. *Adv Electron Mater* 2020, **6**: 1900698.

[22] Nong P, Huang JP, Pan Y, *et al*. Synergistic enhancement of energy storage performance in $NaNbO_3$-based lead-free relaxor ferroelectrics via weakly coupled relaxation behavior. *Small* 2025, **21**: 2406059.

[23] Chen XX, Shen ZH, Liu RL, *et al*. Programming polarity heterogeneity of energy storage dielectrics by bidirectional intelligent design. *Adv Mater* 2024, **36**: 2311721.

[24] Xie AW, Hu TF, Lei JW, *et al*. Local isomeric polar nanoclusters enabled superior capacitive energy storage under moderate fields in $NaNbO_3$-based lead-free ceramics. *Small* 2024, **20**: 2309796.

[25] Chen L, Deng SQ, Liu H, *et al*. Giant energy-storage density with ultrahigh efficiency in lead-free relaxors via high-entropy design. *Nat Commun* 2022, **13**: 3089.

[26] Liu D, Wang L, Wang XY, *et al*. Excellent energy storage performances for $BaTiO_3$-based multilayer capacitors through synergistic high-entropy and superparaelectric-relaxor strategy. *J Materiomics* 2025, **11**: 100860.

[27] Li ZP, Li DX, Shen ZY, *et al*. Remarkably enhanced dielectric stability and energy storage properties in BNT-BST relaxor ceramics by A-site defect engineering for pulsed power applications. *J Adv Ceram* 2022, **11**: 283–294.

[28] Xiong X, Liu H, Zhang J, *et al*. Ultrahigh energy-storage in dual-phase relaxor ferroelectric ceramics. *Adv Mater* 2024, **36**: 2410088.

[29] Li L, Lu S, Cao WJ, *et al*. Band gap engineering and lattice distortion for synergetic tuning optical properties of $NaNbO_3$ toward enhanced piezo-photocatalytic activity. *Inorg Chem* 2024, **63**: 11745–11756.

[30] Tian A, Li ZH, Jiang QK, *et al*. Quasi-antipolar nanoclusters driven superior energy storage in high-entropy relaxor ferroelectrics. *Adv Sci* 2025, **13**: e22801.

[31] Otoničar M, Škapin SD, Jančar B, *et al*. Analysis of the phase transition and the domain structure in $K_{0.5}Bi_{0.5}TiO_3$ perovskite ceramics by in situ XRD and TEM. *J Am Ceram Soc* 2010, **93**: 4168–4173.

[32] Lv X, Chen YB, Wu JG. Temperature-insensitive piezoelectricity in lead-free $NaNbO_3$-based ceramics. *J Am Ceram Soc* 2018, **101**: 5596–5603.

[33] Zhang L, Zhao CL, Zheng T, *et al*. Large electrocaloric response with superior temperature stability in $NaNbO_3$-based relaxor ferroelectrics benefiting from the crossover region. *J Mater Chem A* 2021, **9**: 2806–2814.

[34] Lin DM, Kwok KW. Ferroelectric and piezoelectric properties of new $NaNbO_3$–$Bi_{0.5}K_{0.5}TiO_3$ lead-free ceramics. *J Mater Sci: Mater Electron* 2010, **21**: 1060–1065.

[35] Sun J, Yan GW, Fang BJ, *et al*. Improving energy storage performance of barium titanate-based ceramics by doping MnO_2. *J Energy Storage* 2024, **78**: 110007.

[36] Zhang M, Zheng ZH, Dong FY, *et al*. Ultrahigh energy-storage multilayer ceramic capacitors with low sintering temperature. *Adv Mater* 2026, **38**: e17944.

[37] Shannon RD. Revised effective ionic radii and systematic studies of interatomic distances in halides and chalcogenides. *Acta Cryst A* 1976, **32**: 751–767.

[38] Levin I, Laws WJ, Wang D, *et al*. Designing pseudocubic perovskites with enhanced nanoscale polarization. *Appl Phys Lett* 2017, **111**: 212902.

[39] Xu MZ, Zeng DF, Wang X, *et al*. Optimizing the energy storage performance of $NaNbO_3$ ceramics by rare-earth-based composite perovskite $Sm(Mg_{0.5}Zr_{0.5})O_3$ modification. *Microstructures* 2023, **3**: 2023034.

[40] Wang Y, Li SW, Tong YH, *et al*. Simultaneous enhancement of energy storage and luminescent performances in $Sr_{2-x}Sm_xAg_{0.2}Na_{0.8}Nb_{5-x}Zr_xO_{15}$ multifunctional ceramics. *J Adv Dielectr* 2025, **15**: 2450031.

[41] Peel MD, Thompson SP, Daoud-Aladine A, *et al*. New twists on the perovskite theme: Crystal structures of the elusive phases R and S of $NaNbO_3$. *Inorg Chem* 2012, **51**: 6876–6889.

[42] Zhang MH, Fulanović L, Egert S, *et al*. Electric-field-induced antiferroelectric to ferroelectric phase transition in polycrystalline $NaNbO_3$. *Acta Mater* 2020, **200**: 127–135.

[43] Wei K, Duan JH, Qi H, *et al*. Collaborative design of polarization and antiferrodistortion configurations in high energy capacitive relaxor ferroelectrics. *Nat Commun* 2025, **16**: 7833.

[44] Zhou CP, Yan F, Zheng ZH, *et al*. Achieving superior capacitive energy storage in tape-casting fabricated $Bi_{0.5}Na_{0.5}TiO_3$-based relaxor ferroelectrics via multiscale regulation. *Energy Storage Mater* 2025, **75**: 104082.

[45] Xie AW, Fu J, Zuo RZ, *et al*. Supercritical relaxor nanograined ferroelectrics for ultrahigh-energy-storage capacitors. *Adv Mater* 2022, **34**: 2204356.

[46] Li ZH, Zheng YS, Zhang Y, *et al*. $(Bi_{0.5}Na_{0.5})TiO_3$–$NaNbO_3$–$Bi(Mg_{1/2}Zr_{1/2})O_3$ lead-free relaxor antiferroelectric ceramics featuring ultrahigh temperature-insensitive energy-storage performance. *ACS Appl Mater Interfaces* 2025, **17**: 40690–40698.

[47] Laidler KJ. The development of the Arrhenius equation. *J Chem Educ* 1984, **61**: 494.

[48] Gerstl M, Navickas E, Friedbacher G, *et al*. The separation of grain and grain boundary impedance in thin yttria stabilized zirconia (YSZ) layers. *Solid State Ionics* 2011, **185**: 32–41.

[49] Abdel-Khalek EK, Ibrahim I, Salama TM, *et al*. Structural, optical, dielectric and magnetic properties of $Bi_{1-x}La_xFeO_3$ nanoparticles. *J Magn Magn Mater* 2018, **465**: 309–315.

[50] Weibull W. A statistical distribution function of wide applicability. *J Appl Mech* 1951, **18**: 293−297.

[51] Wang W, Zhang LY, Li C, *et al*. Effective strategy to improve energy storage properties in lead-free $(Ba_{0.8}Sr_{0.2})TiO_3$-$Bi(Mg_{0.5}Zr_{0.5})O_3$ relaxor ferroelectric ceramics. *Chem Eng J* 2022, **446**: 137389.

[52] Jiang J, Meng XJ, Li L, *et al*. Enhanced energy storage properties of lead-free $NaNbO_3$-based ceramics via A/B-site substitution. *Chem Eng J* 2021, **422**: 130130.

[53] Yan F, Bai HR, Ge GL, *et al*. Composition and structure optimized $BiFeO_3$-$SrTiO_3$ lead-free ceramics with ultrahigh energy storage performance. *Small* 2022, **18**: 2106515.

[54] Zubairi H, Lu ZL, Zhu YB, *et al*. Current development, optimisation strategies and future perspectives for lead-free dielectric ceramics in high field and high energy density capacitors. *Chem Soc Rev* 2024, **53**: 10761−10790.

[55] Ning YT, Pu YP, Wu CH, *et al*. Design strategy of high-entropy perovskite energy-storage ceramics: A review. *J Eur Ceram Soc* 2024, **44**: 4831−4843.

[56] Zhang LY, Jing RY, Zhang SJ, *et al*. Multiscale microstructure design for high-performance dielectric energy storage materials. *Microstructures* 2026, **6**: 2026003.

[57] Wang G, Lu ZL, Li Y, *et al*. Electroceramics for high-energy density capacitors: current status and future perspectives. *Chem Rev* 2021, **121**: 6124−6172.

[58] Jayakrishnan AR, Silva JPB, Kamakshi K, *et al*. Are lead-free relaxor ferroelectric materials the most promising candidates for energy storage capacitors? *Prog Mater Sci* 2023, **132**: 101046.

[59] Montecillo R, Chien RR, Tsukada S, *et al*. Excellent capacitive energy storage in bismuth ferrite-based multilayer ceramic. *J Eur Ceram Soc* 2025, **45**: 117694.

[60] Li HT, Li X, Du YX, *et al*. Remarkable energy storage performance of $BiFeO_3$-based high-entropy lead-free ceramics and multilayers. *Chem Eng J* 2024, **499**: 156112.

[61] Lv ZQ, Lu T, Liu Z, *et al*. $NaNbO_3$-based multilayer ceramic capacitors with ultrahigh energy storage performance. *Adv Energy Mater* 2024, **14**: 2304291.

[62] Shi DK, Liu D, Zhao L, *et al*. Achieving ultrahigh energy storage density and efficiency above 90% via reducing defect concentrations for $AgNbO_3$-based multilayer capacitors. *Chem Eng J* 2024, **479**: 147672.

[63] Zhao Y, Meng XJ, Hao XH. Synergistically achieving ultrahigh energy-storage density and efficiency in linear-like lead-based multilayer ceramic capacitor. *Scr Mater* 2021, **195**: 113723.

[64] Bian HR, Zhong H, Liu XH, *et al*. Temperature-insensitive and high-energy storage performance in lead-based antiferroelectric multilayer ceramic capacitors. *Mater Lett* 2025, **382**: 137931.